www.lajss.org
Latin American Journal of Solids and Structures 2 (2005) 5–15

Fast crack growth along interfaces

A. Needleman[a,*], D. Coker[b] and A.J. Rosakis[c]

[a]Division of Engineering, Brown University, Providence, RI 02912, USA
[b]Mechanical and Aerospace Engineering, Oklahoma State University, Stillwater, OK 74078, USA
[c]Division of Engineering and Applied Science, California Institute of Technology, Pasadena, CA 91125, USA

Abstract

Analyses of dynamic crack growth along interfaces are discussed. The material on each side of the bond line is characterized by an elastic constitutive relation. A cohesive surface constitutive relation that allows for the creation of new free surface is also specified across the bond line. The resistance to crack initiation and the crack speed history are then predicted without invoking any additional failure criterion. Two dimensional models, both plane strain and plane stress, of the configuration used in experiments of Rosakis and co-workers are analyzed. The focus is on the emergence of crack speeds greater than a characteristic wave speed and on the nature of crack tip fields at such intersonic crack speeds.

1 Introduction

For remotely loaded cracks in isotropic elastic solids, the energy flux into the crack tip vanishes as the crack speed increases to the Rayleigh wave speed of the material, see [1]. However, theoretical and numerical studies dating back to the mid 1970s, e.g. Andrews [2], Burridge *et al.* [3] and Broberg [4], indicated that faster crack speeds should be possible under shear loading conditions. Because any in-plane loading of a bimaterial interface results in mixed tensile and shear loading conditions near the crack tip, such interfaces were attractive candidates for exploring fast crack growth phenomena and crack growth at intersonic speeds along bimaterial interfaces were first observed experimentally by Liu *et al.* [5], Lambros and Rosakis [6], Singh and Shukla [7]. In principle, intersonic crack speeds are also possible in homogeneous elastic solids under shear loading conditions, but direct experimental evidence for intersonic crack growth in homogeneous elastic solids subject to remote loading was lacking until the work of Rosakis *et al.* [8]. In Rosakis *et al.* [8], a weak plane was introduced directly ahead of a notch tip; in essence constraining the crack to grow in shear mode along the weak plane analogous to interface crack growth in a bimaterial.

* Corresponding author E-mail: Alan_Needleman@brown.edu
Received 03 December 2004
From *Recent Developments in the Modelling of Rupture in Solids Conference*, ed. A. Benallal & S.P.B. Proença.

The near-tip stress and deformation fields vary considerably with the crack speed. This, in turn, plays a major role in determining the apparent fracture toughness of the interface. Since the integrity of structures is generally limited by failure at interfaces, a predictive capability for dynamic crack growth along interfaces underlies the rational design of structures and components where dissimilar materials are joined, particularly under impact loading conditions. In addition, the topic is of basic importance in understanding the dynamics of earthquakes. An overview of interfacial dynamic fracture is given by Rosakis [14].

Here, results are presented from numerical analyses in Needleman and Rosakis [9], Needleman [10] and Coker *et al.* [11], where further references and additional background information are given. The calculations discussed use the cohesive surface decohesion formulation in Needleman [12] and Xu and Needleman [13]. Within this framework, the continuum is characterized by two constitutive relations; one that relates stress and deformation in the bulk material, the other that relates the traction and displacement jump across a cohesive surface. In the analyses discussed, the constitutive relation for the bulk material (or materials) is taken to be that of an elastic solid. The parameters characterizing the cohesive surface separation law include a strength and the work of separation per unit area so that a characteristic length enters the formulation. These constitutive relations together with appropriate balance laws and initial and boundary conditions completely specify the initial-boundary problem. The analyses are two dimensional, plane strain or plane stress, explicit dynamic analyses for initially cracked specimens. The initiation of crack growth and the crack speed history are obtained as natural outcomes of the analysis without any additional assumptions concerning crack initiation or crack growth criteria.

2 Formulation

The formulation considers a continuum that is separated into two domains, the first being volumetric and the second being composed of one or more infinitesimally thin interfaces (cohesive surfaces). The continuum is characterized by two independent constitutive relations: one relating the stress and strain in the bulk material and the other relating the traction and displacement across the cohesive surfaces.

The principle of virtual work is written as

$$\int_V \mathbf{S} : \delta\mathbf{E} dV - \int_{S_{int}} \mathbf{T} \cdot \delta\mathbf{\Delta} dS = \int_{S_{ext}} \mathbf{T} \cdot \delta\mathbf{u} dS - \int_V \rho \frac{\partial^2 \mathbf{u}}{\partial t^2} \cdot \delta\mathbf{u} dV \tag{1}$$

Here, $\mathbf{S}$ is the second Piola-Kirchhoff stress tensor, $\mathbf{u}$ is the displacement vector, $\mathbf{\Delta}$ is the displacement jump across the cohesive surface, $\mathbf{A} : \mathbf{B}$ denotes $A^{ij}B_{ji}$, and V, S_{ext} and S_{int} are the volume, external surface area and internal cohesive surface area, respectively, of the body in the reference configuration. The density of the material in the reference configuration is ρ, $\mathbf{T}$

is the traction vector and the Lagrangian strain, $\mathbf{E}$, is given by

$$\mathbf{E} = \frac{1}{2}(\mathbf{F}^T \cdot \mathbf{F} - \mathbf{I}) \quad , \quad \mathbf{F} = \mathbf{I} + \frac{\partial \mathbf{u}}{\partial \mathbf{x}} \tag{2}$$

with $\mathbf{I}$ the identity tensor and $\mathbf{x}$ denoting the position vector of a material point in the reference configuration.

The volumetric constitutive relation is taken to have the form

$$\mathbf{S} = \mathbf{L} : \mathbf{E} \tag{3}$$

where $\mathbf{L}$ is the tensor of elastic moduli. Orthotropic as well as isotropic materials are considered.

The separation process is taken to be elastic so that the traction across the cohesive surface is a direct function of the displacement jump,

$$\mathbf{T} = -\frac{\partial \phi}{\partial \mathbf{\Delta}} \tag{4}$$

where ϕ is the cohesive potential. An advantage to using (4) is that the work of separation is independent of the path.

The cohesive surface constitutive relation used in the analyses allows for tangential as well as normal decohesion. The key parameters characterizing the cohesive strength are the tensile cohesive strength σ_{max}, the shear cohesive strength τ_{max}, the tensile characteristic length δ_n and the shear characteristic length δ_t.

The normal traction across the surface as a function of the normal displacement jump (with the shear displacement jump zero) is shown in Fig. 1a. The maximum value is σ_{max} and occurs at δ_n. The variation of shear traction with the shear displacement jump (with the normal displacement jump zero) is shown in Fig. 1b. The maximum value is attained when the shear displacement jump across the interface is $\sqrt{2}\delta_t/2$ regardless of its sign. The sign convention is such that restoring tractions are positive.

The normal work of separation, ϕ_n, and the shear work of separation, ϕ_t, are

$$\phi_n = e\sigma_{max}\delta_n \qquad \phi_t = \sqrt{\frac{e}{2}}\tau_{max}\delta_t \tag{5}$$

where $e = \exp(1)$. The cohesive strength and the characteristic length are not necessarily representative of atomistic separation of surfaces, but may model additional small-scale deformations that control the work of separation.

The configuration analyzed is shown in Fig. 2. Both plane strain and plane stress conditions are assumed in the calculations discussed. At $t = 0$, the body is stress free and at rest. A normal velocity is prescribed on a region of width b, either on the crack edge as in Fig. 2 or on the opposite edge, and the shear traction is taken to vanish there. The remaining external surfaces of the specimen are traction free. The prescribed velocity attains the value V_1 with rise time t_r.

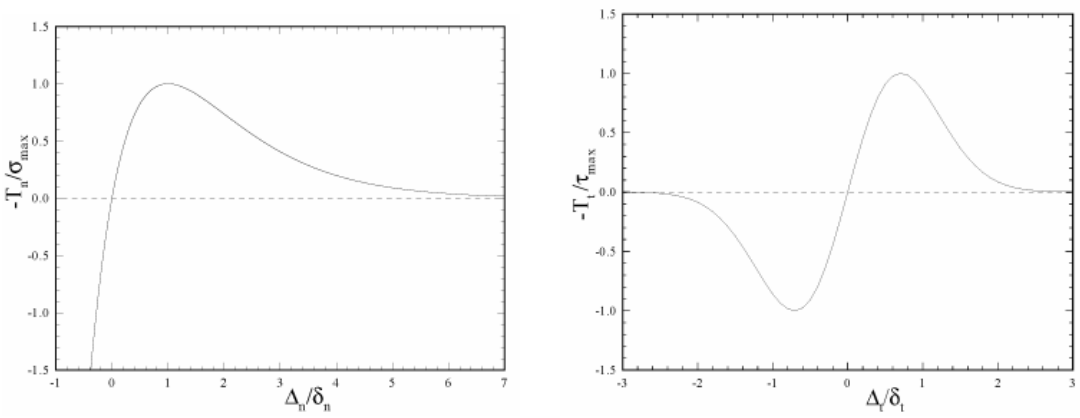

(a) (b)

Figure 1: (a) Normal traction versus normal displacement jump. (b) Shear traction versus shear displacement jump.

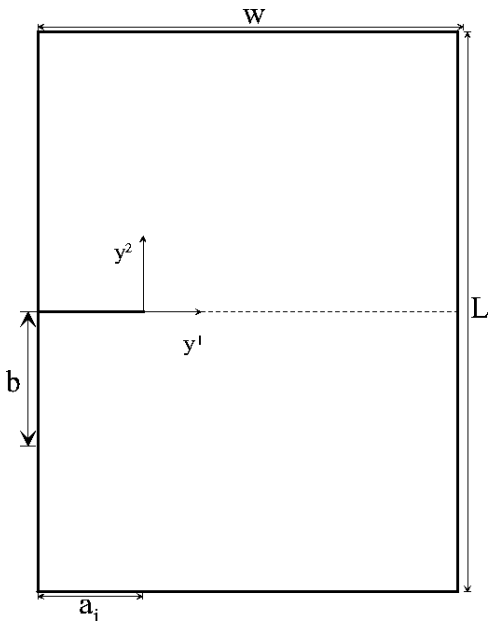

Figure 2: Geometry of the specimen analyzed which is a planar model of the specimen used in experiments by Rosakis and co-workers.

In the calculations to be discussed, the principle of virtual work is discretized based on linear displacement triangular elements arranged in "crossed triangle" quadrilaterals. Fracture initiation and crack growth, including microcrack nucleation ahead of the main crack arise naturally as a consequence of the imposed loading, without any additional assumptions concerning criteria for crack growth, crack path selection or microcrack nucleation.

3 Numerical results

Figure 3, from Needleman and Rosakis [9], shows curves of crack speed versus time for various impact velocities for a particular value of the bond strength of the interface of a PMMA/Steel bimaterial. In [9] a plane strain analysis was carried out. The impact loading takes place on the back surface of the plate (the surface opposite the crack) and the impacter contacts the steel. The main effect of the impact loading is a wave carrying a compressive stress that propagates across the specimen and reaches the crack tip at 16.7 μs. Subsequently, at 25.1 μs the reflected wave reaches the initial crack tip. In some cases in Fig. 3 crack initiation occurs shortly after the initial loading wave has arrived, while in other cases crack growth follows the reflected wave.

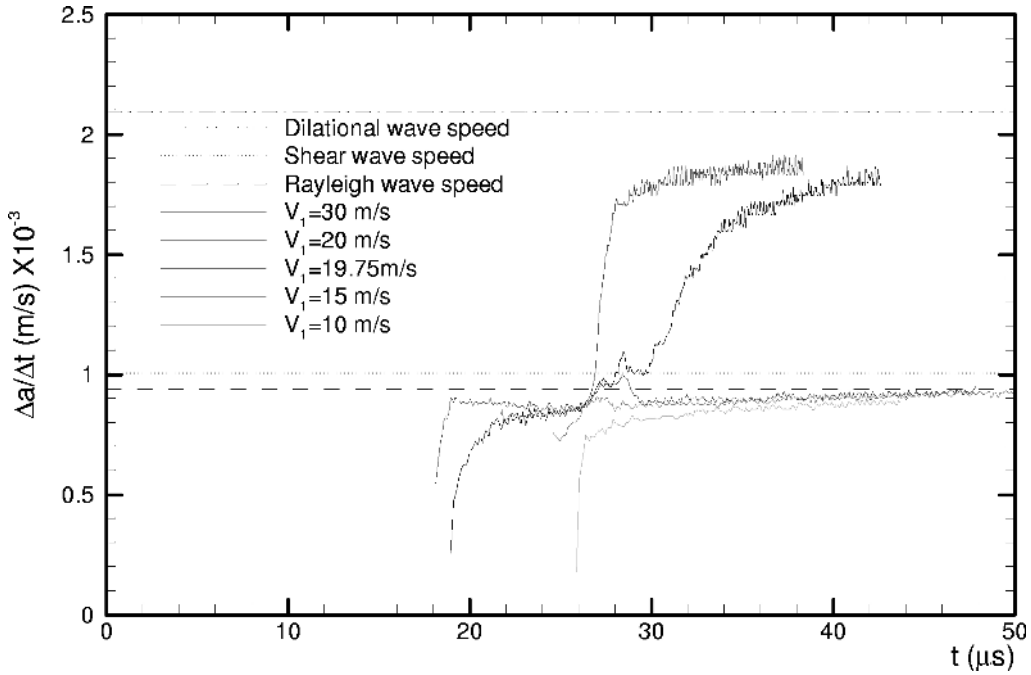

Figure 3: Curves of crack speed, $\Delta a/\Delta t$ versus time, t, for various values of the impact velocity, V_1. The strength of the bond line is specified by $\sigma_{max} = 243$ MPa. From [9].

The most striking feature of the crack growth versus time curves in Fig. 3 is the abrupt

transition between two types of crack growth history. The Rayleigh, shear and dilational wave speeds shown in Fig. 3 are those for PMMA. For a sufficiently low impact velocity, the crack speed approaches the Rayleigh wave speed of PMMA (938 m/s), while if the impact velocity is above a transition value the mean crack speed increases to about 1800 m/s. The transition impact velocity in Fig. 3 is between 19.75 m/s and 20 m/s. With $V_1 = 19.75$ m/s crack growth begins at 21.6 μs. The crack speed increases to 995 m/s at $t = 28.4$ μs, falls to 885 m/s and then slowly increases to about the Rayleigh speed of PMMA. When the impact velocity is increased to 20 m/s, crack growth begins slightly earlier and follows essentially the same trajectory as with an impact velocity of 19.75 m/s until $t = 28.4$ μs. The crack speed then continues to increase to a local maximum of 1059 m/s at 28.7 μs, and then decreases to 995 m/s at $t = 29.5$ μs. This jump in crack speed is associated with the arrival of the reflected wave in the vicinity of the crack tip. Increasing the impact velocity to 30 m/s gives rise to earlier crack growth and a steeper rise to a crack speed that is very close to the one reached with $V_1 = 20$ m/s. A similar sharp transition impact velocity was found in Needleman and Rosakis [9] for a broad range of values of the bond line cohesive strength.

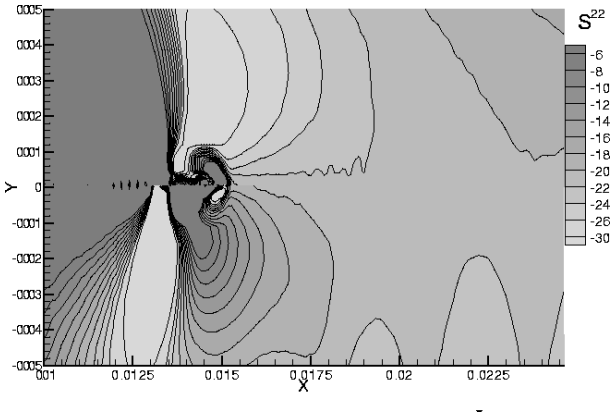

Figure 4: Contours of the opening stress component showing the emergence of a microcrack ahead of the main crack. The calculation is for homogeneous Homalite with a weak plane directly ahead of the initial crack tip. From [10].

The transition from a subsonic to an intersonic crack speed can involve microcrack nucleation ahead of the main crack. The contour plot of the opening stress component, S^{22}, shown in Fig. 4, for a homogeneous Homalite plate with a weak plane in the plane of the crack from Needleman [10], illustrates the nucleation of a microcrack ahead of the main crack facilitating the transition to an intersonic crack speed.

Figure 5, from Needleman and Rosakis [9], shows crack growth results for two meshes. In Fig. 5, the two curves are in very good agreement while the crack speed is below the PMMA Rayleigh wave speed. The rapid increase in crack speed occurs about 1.1 μs later and more abruptly for

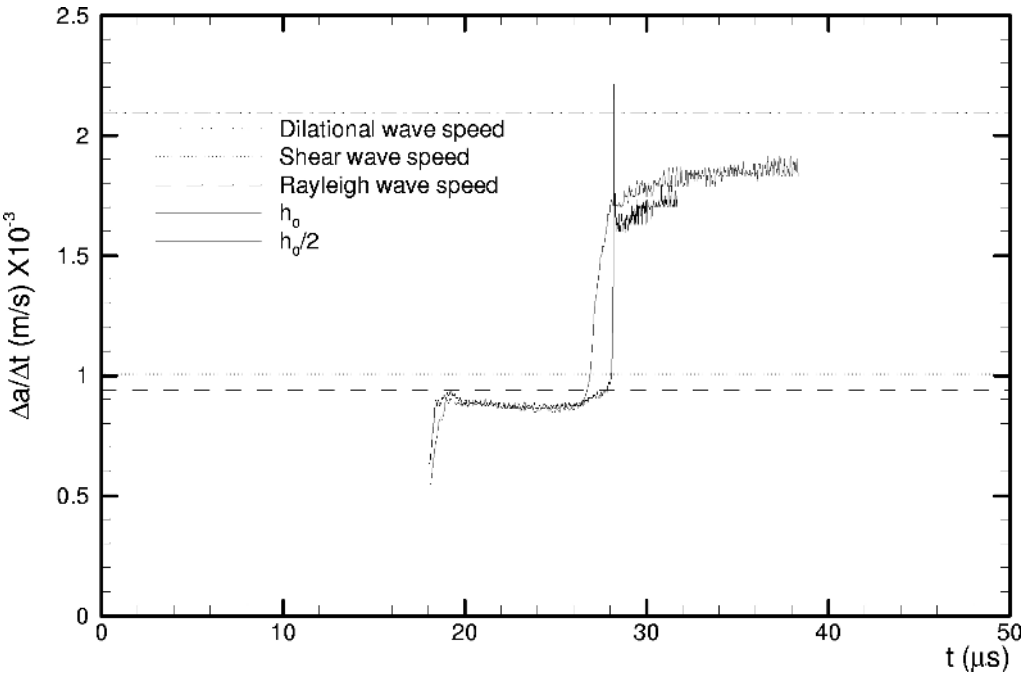

Figure 5: Curves of crack speed, $\Delta a/\Delta t$ versus time, t, for two meshes. In the h_0 mesh the uniform grid spacing on the bond line is 75 μm, while in the $h_0/2$ mesh it is 37.5 μm. From [9].

the finer mesh. Once, the crack speed jump has occurred, the mean crack speed for the finer mesh calculation is about 6% less than that for the calculation using the reference h_0 mesh. With a lower bond strength, not shown here, the crack speed versus time curves are virtually identical except for an increased oscillation amplitude with the finer mesh. Since gradients near the crack tip essentially scale with E/σ_{max} times the cohesive characteristic length, see e.g. Morrisey and Rice [15], more accurate results are expected for lower strength bond calculations with a given mesh spacing.

Coker *et al.* [11] have carried out a combined experimental-numerical study of intersonic crack growth along an interface between a unidirectional graphite fiber reinforced epoxy composite and Homalite. In [11] plane stress analyses were carried out. The unidirectional composite is highly anisotropic (orthotropic symmetry). The Rayleigh, shear and longitudinal wave speeds for Homalite are 1155 m/s, 1255 m/s and 2187 m/s, respectively, while the corresponding wave speeds for the composite are 1548 m/s, 1560 m/s and 7380 m/s, which is the longitudinal wave speed parallel to the fibers. Thus, there is a large mismatch in longitudinal wave speeds, but the other relevant elastic wave speeds have comparable magnitudes.

The loading cases analyzed are shown in Fig. 6 together with a schematic of the induced loading waves.

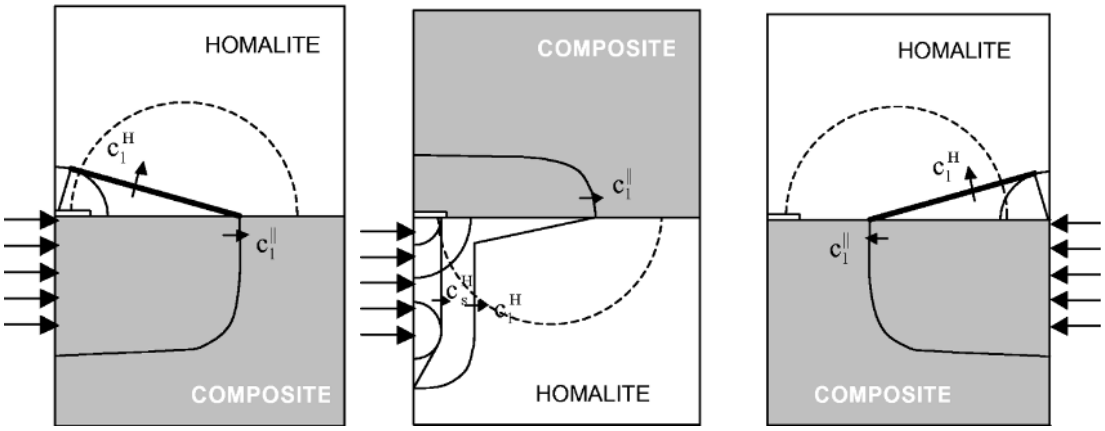

(a) (b) (c)

Figure 6: Three configurations used in [11] to investigate crack speed regimes in the Homalite-composite bimaterial and schematic of the loading waves in the specimen. (a) case 1. (b) case 2. (c) case 3.

Figures 7 and 8 compare measured and predicted crack speeds for case 1 and case 3, respectively. For case 2 neither the experiments nor the calculations gave rise to intersonic crack speeds. There is very good agreement between the character of the crack speed histories in all three cases. However, the predicted impact velocities for achieving a given crack speed history are quite different from those observed. This may be because the calculations are carried out for an initially sharp crack whereas there is an initial rounded notch in the experiments. Another possible factor contributing to the discrepancy is that the value used for the bond cohesive strength may not be representative of that in the experiments.

Computationally, sustained crack speeds at the longitudinal wave speed of the composite are attained for both case 1 and case 3. However, the direction of relative sliding is opposite in these two cases; in case 1 the composite slides in the crack growth direction, whereas in case 3 the Homalite slides in the crack growth direction. When this sustained crack speed is attained in case 1, the normal tractions directly ahead of the crack tip are compressive, whereas at this speed in case 3 the normal tractions are tensile. Conversely, when the sustained crack speed is between the Rayleigh and longitudinal wave speeds of Homalite, the normal tractions directly ahead of the crack tip are tensile in case 1 and compressive in case 3. The results suggest that there is a crack speed at which the normal traction (and displacement jump) change sign, with the sense of the change depending on the sliding direction.

As in Needleman and Rosakis [9] and Needleman [10], sustained crack speeds are found to be possible only in discrete ranges. In particular, intersonic crack speeds between $\sqrt{2}$ times the shear wave speed of the material with the slower elastic wave speeds and the fastest wave speed

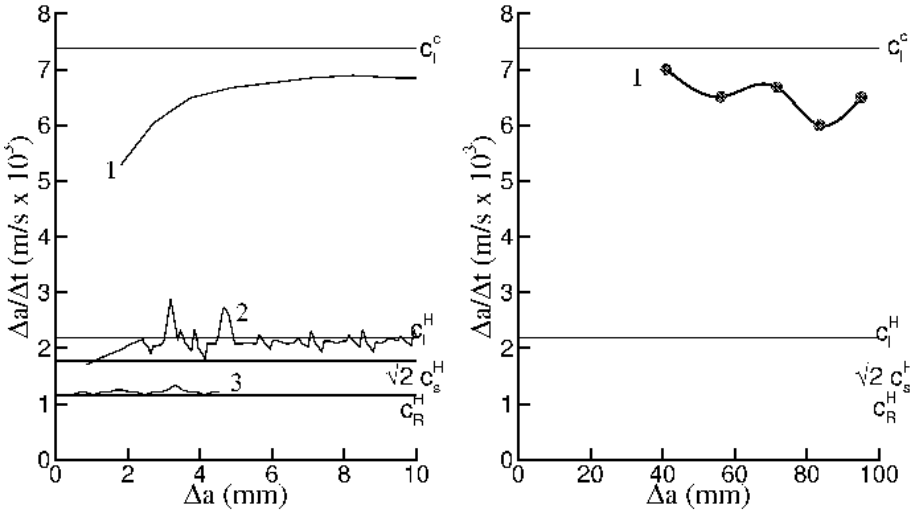

Figure 7: Comparison of numerically predicted and experimentally measured crack speed histories for case 1. Curves 1-3 of the numerical results are for impact speeds of 20, 10 and 5 m/s, respectively. The experimental result is for an impact speed of 35 m/s. From [11].

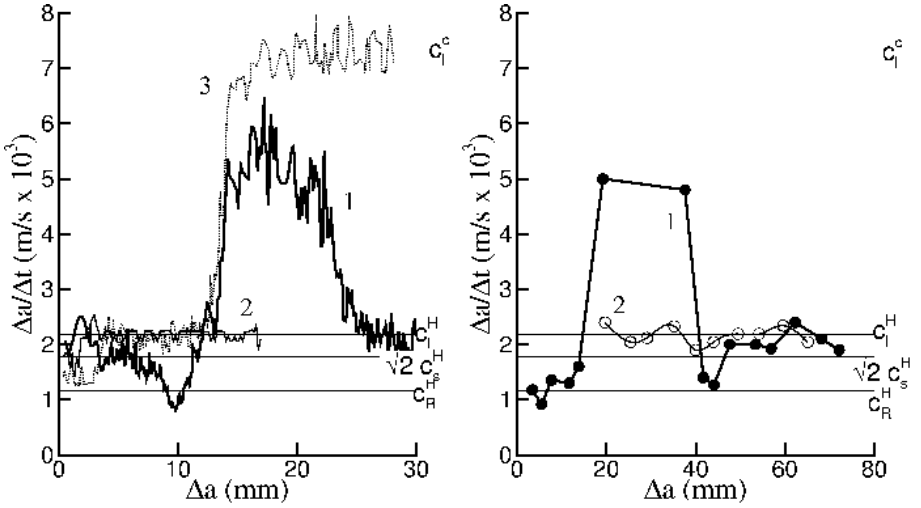

Figure 8: Comparison of numerically predicted and experimentally measured crack speed histories for case 3. Curves 1-3 for the numerical results are for impact speeds and impact times of (20 m/s, 3 μ s), (15 m/s, 10 μs), and (10 m/s, 25 μs), respectively. Experimental curves 1-2 are for impact speeds of 40 and 27 m/s, respectively. From [11].

of the material with the higher elastic wave speeds are seen.

Contours of the difference between the two in-plane principal stresses are shown in Fig. 9 for case 1 where the crack speed exceeds the longitudinal wave speed of Homalite. These contour lines are what the fringe lines observed experimentally represent, thus permitting a direct comparison between computation and experiment. The calculations and the experimental observations agree in remarkable detail (see Coker *et al.* [11]). For example, both the outer fringe lines and the inner fine structure are seen in the experiments. This fringe pattern arises because the crack speed exceeds all characteristic elastic wave speeds of Homalite. The predicted fringe patterns vary substantially with the impact conditions and the predicted variation between the three loading cases is consistent with what is seen in the experiments. The calculations in Coker *et al.* [11] contain no fitting parameters; the strength of the bondline is assigned based on an independent estimate of the glue strength. Furthermore, the calculations are actual predictions and, in fact, were, in some cases, used in the experimental design.

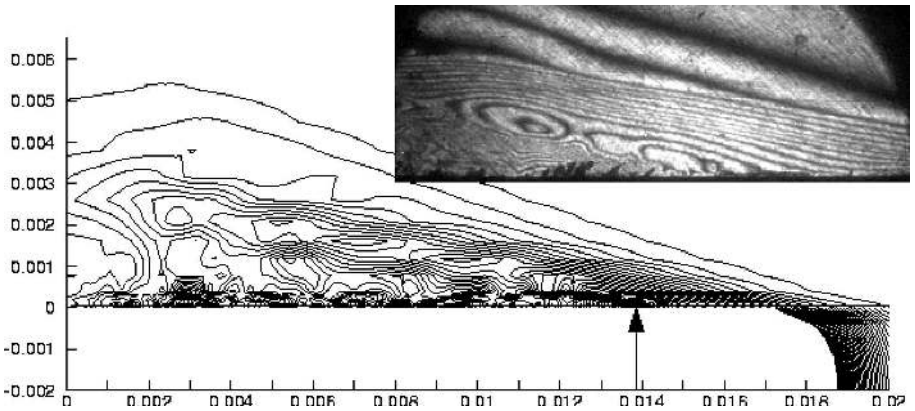

Figure 9: Contours of the difference between the maximum and minimum in-plane principal stresses for case 1 loading with the crack speed ≈ 7300 m/s. The insert shows the experimentally observed fringe pattern. From [11].

Among the conclusions of Coker *et al.* [11] are that sustained crack growth occurs within discrete speed ranges delimited by characteristic elastic wave speeds and that the greatest longitudinal wave speed appears to provide the upper limit to the sustainable crack speed. Not all of the numerically predicted regimes were seen in the experiments. In the computations, the crack was forced to grow along the bond line; one possibility is that the tendency for the crack path to deviate from the bond line is so strong in some regimes that their experimental realization is effectively precluded, at least for the bimaterial system considered in [11].

References

[1] L. B. Freund. Dynamic Fracture Mechanics, Cambridge University Press, Cambridge, 1998.

[2] D. J. Andrews. Rupture Velocity of Plane Strain Shear Cracks, J. Geophys. Res., 81:5679–5687, 1976.

[3] R. Burridge, G. Conn, and L. B. Freund. The Stability of a Rapid Mode II Shear Crack with Finite Cohesive Traction, J. Geophys. Res., 85:2210–2222, 1979.

[4] K. B. Broberg. The Near-Tip Field at High Crack Velocities, Int. J. Fract., 39:1–13, 1989.

[5] C. Liu, J. Lambros, and A. J. Rosakis. Highly Transient Elasto-Dynamic Crack Growth in a Bimaterial Interface: Higher Order Asymptotic Analysis and Optical Experiment, J. Mech. Phys. Solids, 41:1887–1954, 1993.

[6] J. Lambros and A. J. Rosakis. Shear Dominated Transonic Interfacial Crack Growth in a Bimaterial-I. Experimental Observations, J. Mech. Phys. Solids, 43:169–188, 1995.

[7] R. P. Singh and A. Shukla. Subsonic and Intersonic Crack Growth Along a Bimaterial Interface, J. Appl. Mech., 63:919–924, 1996.

[8] A.J. Rosakis, O. Samudrala, and D. Coker. Cracks Faster than the Shear Wave Speed, Science, 284:1337–1340, 1999.

[9] A. Needleman and A. J. Rosakis. The Effect of Bond Strength and Loading Rate on the Conditions Governing the Attainment of Intersonic Crack Growth Along Interfaces, J. Mech. Phys. Solids, 47:2411–2449, 1999.

[10] A. Needleman. An Analysis of Intersonic Crack Growth under Shear Loading, J. Appl. Mech., 66:847–857, 1999.

[11] D. Coker, A. J. Rosakis, and A. Needleman. Dynamic Crack Growth Along a Polymer Composite-Homalite Interface, J. Mech. Phys. Solids, 51:425–460, 2003.

[12] A. Needleman. A Continuum Model for Void Nucleation by Inclusion Debonding, J. Appl. Mech., 54:525–531, 1987.

[13] X.-P. Xu and A. Needleman. Numerical Simulations of Fast Crack Growth in Brittle Solids, J. Mech. Phys. Solids, 42:1397–1434, 1994.

[14] A. J. Rosakis. Intersonic Shear Cracks and Fault Ruptures, Adv. Phys., 51:1189–1257, 2002.

[15] J. W. Morrisey and J. R. Rice. Crack Front Waves, J. Mech. Phys. Solids, 46:467–488, 1998.